Microwave spectroscopy of high-L helium Rydberg states: $10H$-$10I$, $10I$-$10K$, and $10K$-$10L$ intervals

E. A. Hessels, W. G. Sturrus, and S. R. Lundeen
Department of Physics, University of Notre Dame, Notre Dame, Indiana 46556
(Received 5 May 1988)

Fine-structure intervals separating the $10H$ ($L=5$), $10I$ ($L=6$), $10K$ ($L=7$), and $10L$ ($L=8$) states of helium have been measured precisely, using a fast-beam microwave–laser resonance technique. The results: $10H$-$10I$, 157.0508(26) MHz; $10I$-$10K$, 60.8152(18) MHz; and $10K$-$10L$, 27.1835(63) MHz agree well with theoretical predictions which include contributions due to "retardation" or "Casimir" forces.

I. INTRODUCTION

Precise spectroscopy of high-angular-momentum ($L \geq 4$) Rydberg states of the helium atom offers a number of opportunities to test fundamental aspects of the theory of two-electron atoms. The particular advantage of the high-L $(1s)(nL)$ states for this purpose is their relatively simple wave functions, which approach the limit of nonoverlapping purely hydrogenic orbitals for *both* electrons as L increases. Because of this, they can be understood theoretically with very high precision. The structure of the high-L states is characterized by four approximately equally spaced levels for each value of L, as illustrated in Fig. 1 for the states of interest here. We refer to the fourfold structure of common L as "magnetic fine structure" (MFS), since it is produced largely by spin-dependent magnetic interactions. This structure has been studied experimentally for the $n=10$ G and H states,[1] where it was found to agree with theoretical predictions to within the 0.1% precision of the measurements. The numerical values of the MFS shown in Fig. 1 are taken from the calculations described in Ref. 1. The fine-structure intervals separating states of different L, and in particular the unique intervals which would be observed in the absence of spin and exchange interactions, are referred to as "electric-fine-structure" (EFS) intervals. The values shown in Fig. 1 are taken from the calculations of Drachman.[2] Since the exchange interactions are extremely small for the high-L states, the two MFS levels with $J=L$ are not even approximately eigenstates of total electron spin, but approach the limit of equal mixtures of singlet and triplet states as L increases. Because of this, we refer to these states by the nonstandard notation ${}^{\pm}L_L$, as shown in Fig. 1, to avoid confusion which can be caused by the inappropriate usage of standard LS coupling notation.

While extensive microwave spectroscopy of lower-L helium Rydberg states has been carried out by Wing and his collaborators,[3] the first experimental studies of the higher-L states were obtained by Beyer and Kollath, using a level anticrossing technique.[4] Later, rf spectroscopy of considerably higher precision was reported for a few such states by Cok and Lundeen, using a fast-atomic-beam technique based on detection of the states by their cascading optical fluorescence.[5] Palfrey and Lundeen developed a laser-based detection scheme, suitable for studying $n=10$ helium Rydberg states, and used it to improve the precision of the measurements further and extend them to higher L.[6] The measurements reported

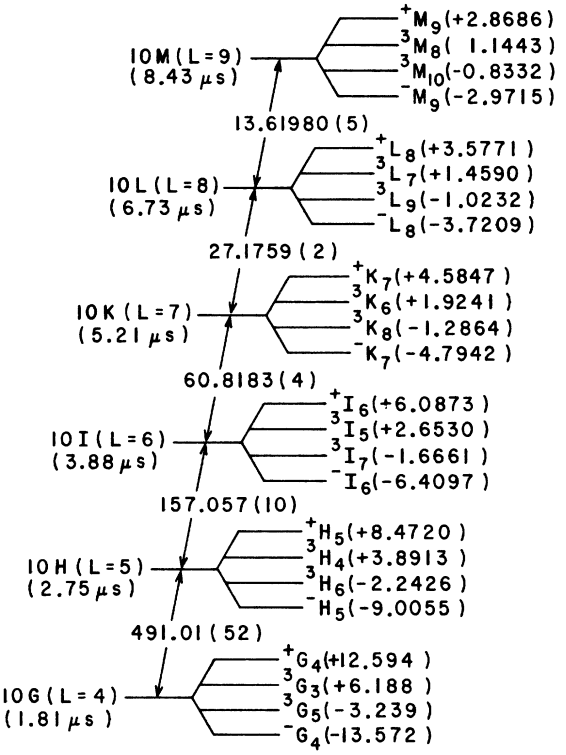

FIG. 1. Energy-level diagram for the high-L states of $n=10$ helium. The values of the electric-fine-structure splittings (the splitting between states of different L) are taken from Drachman (Ref. 2). The values of the magnetic-fine-structure splittings (the splittings within a single L) are taken from Ref. 1. The exchange energy is taken to be zero for states with $L>4$. The states are labeled ${}^{2S+1}L_J$ except for the two states with $J=L$, ${}^{\pm}L_J$, which are approximately equal mixtures of singlet and triplet states. The energy separations are given in MHz and are not drawn to scale. The radiative lifetime for each state is given in parentheses.

here use an improved version of the same technique which gives yet higher precision and allows the study of the highest-L states of $n=10$.

One of the aims of this high-L spectroscopy is to achieve a detailed test of the influence on the level positions of "retardation" or "Casimir" forces.[7,8] These are nonclassical long-range electromagnetic interactions arising from the exchange of photons, at least one of which is transverse. They are closely related to the Casimir-Polder interaction,[9] which dominates the long-range interaction between neutral atoms and to the "Casimir force" of attraction between neutral conductors.[10] Like these related forces, the "retardation" forces in the helium atom may be considered to result from the action of zero-point photons of the electromagnetic field.[11] None of these forces has yet been subjected to precise experimental tests.

In 1978, Kelsey and Spruch predicted that the effect of such "retardation" forces gives an additional interaction between a Rydberg electron and a polarizable ion core given by

$$V_{\mathrm{KS}}=\frac{11}{4\pi}\left[\frac{\hbar}{mc}\right]\frac{e^2\alpha_d}{r^5}\ , \tag{1}$$

where α_d is the dipole polarizability of the ion core, $\hbar/mc$ is the electron's Compton wavelength, and r is the radial coordinate of the Rydberg electron.[7] This simple form of the "retardation" interaction is expected to be valid only at large r ($r\geq 137a_0$). Spruch and Kelsey also suggested that the presence of such an interaction could be tested by precise measurements of fine-structure intervals separating high-L Rydberg states of helium, where other contributions to the structure could be very precisely calculated. The effect could not be seen in the existing spectroscopy of lower-L states because of the limited precision of available calculations.[12] At higher L, however, the extended polarization model of Drachman[2] led to theoretical predictions of the Rydberg electric-fine-structure intervals which were considerably more precise than the expected contributions due to "retardation forces." The first experimental test based on these calculations[6] concluded that any contributions to the structure of high-L $n=10$ Rydberg states of helium from the "retardation forces" were considerably smaller than suggested by Eq. (1). More detailed calculations of the "retardation" effects reached the same conclusion and made specific predictions for the expected contributions to $n=10$ states, which are about an order of magnitude smaller than the expectation value of Eq. (1).[8,13] Given the smaller size of the predicted effects, a clear test using the polarization model calculations can only be achieved at even higher L. We report here the results of such measurements for the $10H$-$10I$, $10I$-$10K$, and $10K$-$10L$ intervals. The result for the $10I$-$10K$ interval gives a weak confirmation (1.7σ) of the presence of the "retardation" effects.

Section II describes the experimental method used to observe these high-L fine-structure transitions. Section III describes the measurements from which the actual results are inferred, including discussion of systematic corrections. Section IV discusses the results and their implications.

II. EXPERIMENTAL METHOD

Figure 2 illustrates the apparatus used for these measurements, which is similar to that described in Ref. 6. A fast beam of neutral helium is formed from a beam of He^+ ions, of about 11-keV energy, which undergoes charge-exchange neutralization in a gas cell containing about 0.05 torr of argon gas. Many of the neutral atoms are formed in excited Rydberg states. Those in states with $n=10$ may be conveniently detected by resonant excitation with a Doppler-tuned CO_2 laser to a higher Rydberg level, typically $n=27$, which is near enough to the ionization limit to be easily Stark ionized. The resulting He^+ ions can be collected with high efficiency in a channel electron multiplier. The laser excitation is nearly Doppler-free because of the close collimation of the initial ion beam, thus allowing selective detection of individual angular momentum states in the $n=10$ Rydberg manifold. This two-step detection process takes place at (8) and (9) in Fig. 2. The background rate, in the absence of the laser, due to Stark ionization of Rydberg atom initially formed in states with $n\geq 24$ can be eliminated by Stark ionizing these states immediately after charge exchange, at (3) in Fig. 2, and deflecting the resulting ions out of the beam, along with the residual charged com-

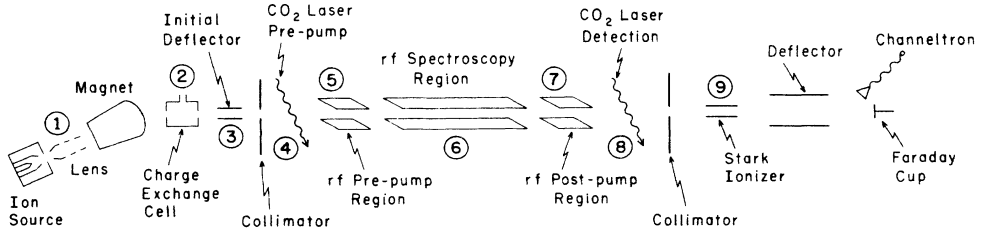

FIG. 2. Schematic of the experimental setup. A beam of 11-keV ions is created, focused, and bent by the source, lens, and magnet, respectively. Part of the beam is neutralized at (2) and the remainder is deflected out of the beam at (3). The rf spectroscopy is done in the meter-long region at (6). The laser at (4) and the pre-pump region at (5) are used to set up an initial population difference. The components from (7) to the end of the beamline serve as a detector of rf transitions. The $n=10$ states are selectively excited to $n=27$ states by the post-pump region at (7) and the laser at (8). These $n=27$ states are then Stark ionized at (9) and deflected into a channeltron detector. Details of the experimental setup are given in Sec. II of the text.

ponent of the initial ion beam.

A typical $n = 10$-to-$n = 27$ laser-excitation spectrum is shown in Fig. 3. Excitation of $10G$ and $10H$ states give resolved resonances which are apparent in the spectrum. Higher-L states are also present with approximately statistical weights, but unresolved in the spectrum. The excitation linewidth ($\cong 170$ MHz) is due to a combination of the angular width of the fast atomic beam ($\cong 0.002$ rad) and transit time and power-broadening width of the homogeneous laser excitation line shape. Figure 4 shows the construction of the Doppler-tuned laser interaction region and of the Stark ionization detector and lists typical parameters for operation of these components.

High-resolution rf spectroscopy of transitions among different $n = 10$ fine-structure levels can be obtained by using the laser-induced ion current to monitor the population of one of the levels (e.g., the $10H$ state) while inducing rf transitions between that state and a nearby level (e.g., the $10I$ state). Given an initial population difference between the two levels, the resonant rf transition leads to a change in population of the detected level and therefore to a change in the detected ion current. The initial population difference can be ensured by deliberately depleting the population of one to the levels involved in the transition by means of an additional laser-excitation transition induced at (4) in Fig. 2. In practice, this is done by simply splitting the laser beam and causing it to intersect the atomic beam twice.

The rf transition is induced in a meter-long interaction region at (6) in Fig. 2. This device is fabricated as a section of TEM transmission line by adding an inner conductor to a section of WR229 waveguide. The geometry, illustrated in Fig. 5, is such as to give a TEM impedance near 50 Ω and an electric field along the atomic-beam trajectory of about 0.3 V/cm for a TEM traveling wave intensity of 1 W. The impedance match at the entrance and exit of the transmission line was studied by measuring the reflection coefficient which it produces in a 50-Ω coaxial line when the exit port is terminated in a nearly perfect load. The results of such measurements, over the frequency range 10–1000 MHz, could be largely accounted for by assuming a constant resistive mismatch giving a

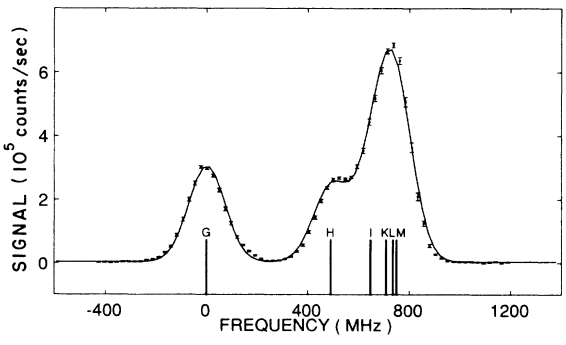

FIG. 3. Laser excitation spectrum. The vertical bars show (from left) the $n = 10$ G, H, I, K, L, and M to $n = 27$ laser resonance positions. The spectrum was taken by Doppler tuning the CO_2 laser. The horizontal scale gives the frequency difference in MHz from the $10G$ peak.

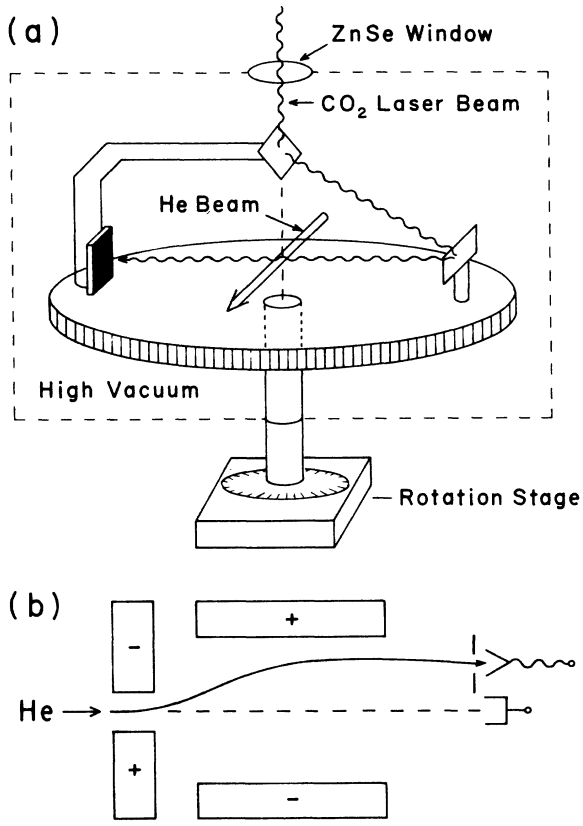

FIG. 4. Experimental apparatus. One of the laser interaction regions is shown in (a). A laser beam of radius 5 mm and power of 10 W was used in each of the laser interaction regions. The frequency of the laser was Doppler tuned by changing the intersection angle. A diagram of the stripper and deflector is shown in (b). The electric field was approximately 2000 V/cm between the stripper plates and 100 V/cm between the deflector plates.

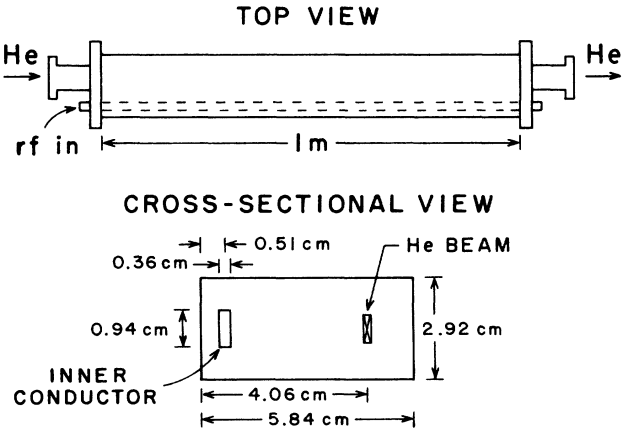

FIG. 5. The central rf interaction region. The region is a TEM transmission line which has been constructed from a section of WR229 waveguide with an inner conductor inserted.

reflection coefficient at each end of the line of magnitude 0.15. In operation, the exit port of the interaction region was terminated with a precision attenuator (Weinschel Engineering model 1-10) followed by an rf power meter (Hewlett-Packard Model 435B/8581A). As the rf frequency was varied, its amplitude was adjusted to give a constant reading on the power meter. The entire length of the rf interaction region was enclosed in a two-layer cylindrical μ-metal magnetic shield in order to eliminate the Earth's magnetic field. The residual magnetic field within the region was measured to be less than 0.01 G.

Figure 6(a) shows the spectrum of rf transitions between the 10H and 10I states observed when both laser interactions of Fig. 2 are tuned to excite the 10H state. In this configuration, the ion current is proportional to the population of the 10H state and the initial population of the 10I state exceeds that of the 10H state. Thus an increase in ion current is observed when the rf frequency matches the 10H-10I transition. The plotted signal is the ac component of the ion current synchronous with a 100% square-wave modulation of the rf intensity. The rf electric field for this transition was adjusted to about 0.0050 V/cm and held constant across the line. The four-peaked structure is due to the magnetic fine structure (MFS) of the 10H and 10I states, illustrated in Fig. 1. The four resonance peaks correspond to transitions between "corresponding" levels in the two manifolds (i.e., $^{+}H_5$-$^{+}I_6$, etc.). The resonance linewidth is dominated by the transit width (0.661 MHz) due to the 1.34-μsec transit time of the atomic beam through the transmission line.

Rf transitions among higher-L states cannot be observed with the scheme described above, since the states involved are unresolved in the laser excitation. A simple extension of the method, however, makes it possible to observe these transitions. Two additional rf interaction regions, referred to as the "pre-pump" and "post-pump" regions and located at (5) and (7) in Fig. 2, are used to manipulate the populations of the higher-L levels in order to achieve the necessary initial population differences and differential detection. For example, the 10I-10K transition, shown in Fig. 6(b), is observed with both lasers tuned to excite the 10H state and with each of the rf pump regions adjusted to the frequency and power appropriate to approximately invert the 10H and 10I populations via the 10H-10I transition. With this configuration, the initial population of the 10K state exceeds that of the 10I state, and the ion current is largely due to the population of the 10I state emerging from the primary rf interaction region. Similarly, the 10K-10L transition, illustrated in Fig. 6(c), is observed with the lasers tuned again to excite the 10H state, but with the pump fields adjusted to invert the populations of the 10H and 10K states via the two-photon 10H-10K rf transition. For both of these transitions, the four MFS components do not appear with statistical weights in the spectrum, since the choice of frequency for the pump transitions discriminates between the MFS components of the pump transitions. For example, the spectrum of Fig. 6(c) is observed with the frequencies of these pump fields chosen to be 112.0 MHz, which leads to an rf spectrum dominated by the $^{-}K_7$-$^{-}L_8$ transition. The two-photon 10K-10M

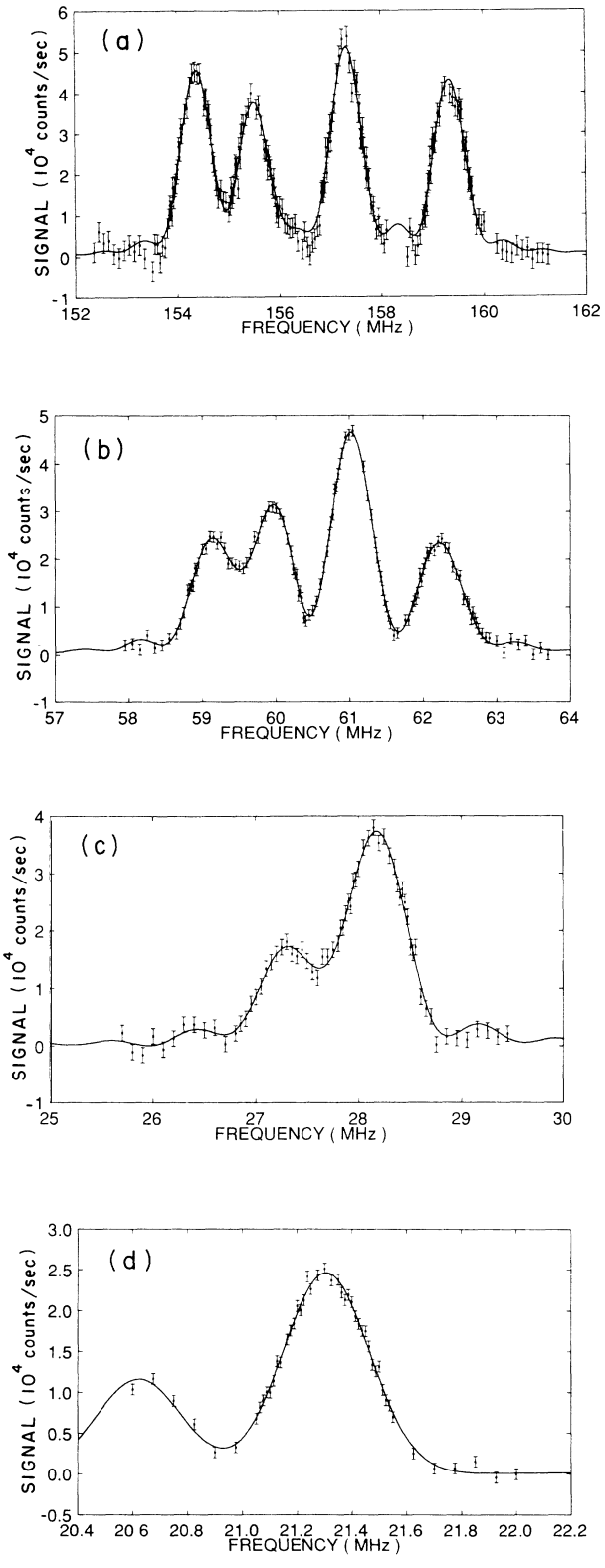

FIG. 6. Typical rf resonance spectra. Spectra of the three measured intervals, the 10H-10I, 10I-10K, and 10K-10L, are shown in (a), (b), and (c), respectively. The particular two-photon 10K-M resonance which was used to monitor the stray electric field (the $10^{-}K_7 - 10^{-}M_9$) is shown in (d). The data points in (a) represent 1 min of data time while the points in the other scans represent 6 min.

transition [see Fig. 6(d)], which is used to study stray electric fields because of its extreme sensitivity to Stark shifts, is observed with the same configuration used to observe the $10K$-$10L$ transition, but with a higher rf power in the central meter-long interaction region. Both of the rf pump regions are also enclosed in magnetic shields, to eliminate motional electric fields which would otherwise Stark broaden the transitions. The pre- and post-pump regions are driven by separate oscillators to avoid distortions of the line shape produced in the central region which would result from coherent effects. The resonance linewidths for these regions were about 10 MHz, as determined by the beam transit times through the regions. Table I summarizes the conditions under which the four transitions of interest are obtained in this experiment.

In general, the predicted resonance structure for these transitions consists of four strongly allowed transitions, connecting "corresponding" states of the two MFS manifolds, and a number of other weaker transitions. These weaker transitions were studied in Ref. 1. At the power levels used in this experiment, their influence on the spectrum is negligible. Thus we expect four peaks whose relative positions are controlled by the MFS and whose relative intensities are to some extent adjustable by the experimental conditions. Each of these is in turn a superposition of degenerate resonances arising from states of different m_J. We therefore assume that the measured signal is of the form

$$S(\nu)=\sum_{\kappa=1}^{4}\sum_{m}P(\kappa,m)S_m^0(\nu-\nu_{\rm EFS}^0-\Delta_{\rm MFS}^\kappa)\ , \tag{2}$$

where the index κ indicates the four transitions, $\Delta_{\rm MFS}^\kappa$ is the contribution due to magnetic fine structure, m runs over the possible values of m_J, and $S_m^0(\Delta\nu)$ is the two-level resonance line shape[14] for a uniform rf field of duration T. If T is very long compared to the radiative lifetimes of the states involved in the resonance, the width of the resonance approaches a limit determined by the *difference* of the decay constants of the two states. For instance for the $10H$-$10I$ transition,

$$\Gamma_{HI}^{\rm nat}=\frac{1}{2\pi}(1/\tau_H-1/\tau_I)=17\ \text{kHz}\ ,$$

using the radiative lifetimes shown in Fig. 1. For the present experiment, the transit time T is sufficiently short ($T\cong 1.34\ \mu$sec) so that the lineshape is much broader than this limiting width. In fact, its shape is not expected to differ significantly from the shape that would be observed if both the levels involved were stable. Since this function is much simpler than that which includes radiative decay, we use it to fit the resonances and take

$$S_m^0(\nu-\nu^0-\Delta^\kappa)=(2V/B)^2\sin^2(\pi BT)\ , \tag{3}$$

where

$$V=\frac{e\,|E_0|}{2h}\langle 10L,\kappa,m\,|\,z\,|\,10(L+1),\kappa,m\rangle\ ,$$

$$B=[(2V)^2+(\nu-\nu^0-\Delta_\kappa)^2]^{1/2}\ ,$$

and $|E_0|$ is the amplitude of the (uniform) rf electric field inside the interaction region.

The dependence of the line-shape function S^0 on m is due only to the dependence of the dipole matrix elements on m. For convenience, we choose to use a fitting function derived from a single m state, and study separately the possible effects on the line shape from the distribution of m states. Thus we take as a model of the experimental line shape

$$S(\nu)=\sum_{\kappa=1}^{4}P(\kappa)S_{m=3}^0(\nu-\nu^0-\Delta^\kappa)\ . \tag{4}$$

The smooth curves in Fig. 6 are fits of experimental data with a function of this form.

Major systematic effects

Two systematic effects were of sufficient importance so that they dictated the manner in which data could be taken for precision determination of the EFS intervals. The most troublesome is the possibility of Stark shifts of the resonance positions due to the presence of small stray electric fields within the primary rf spectroscopy region. In earlier experiments with this technique,[1,6] dc electric fields as large as 100 mV/cm rms were observed to build up gradually within this region, presumably due to charging of nominally conducting surfaces. The existence of these fields could be inferred from studies of the relative Stark shifts of several EFS resonances, and separately by studies of Stark-assisted one-photon fine-structure transitions such as $10H$-$10K$ and $10K$-$10M$, which occur only in the presence of stray fields.[15] For the present measurement, the size of these fields was successfully reduced by gold plating the center conductor of the interaction region, and by collimating the neutral beam more carefully. Even with these improvements, the size of the stray field varied somewhat throughout the experiment, perhaps due to variations in beam alignment. Under favorable circumstances, however, stray fields as low as 10 mV/cm

TABLE I. Conditions for the observations of each of the EFS intervals.

EFS Interval	Number of photons	rf pump transition	Laser setting	rf power
$10H$-$10I$	1	None	H peak	300 μW
$10I$-$10K$	1	H-I (1γ)	H peak	400 μW
$10K$-$10L$	1	H-K (2γ)	H peak	500 μW
$10K$-$10M$	2	H-K (2γ)	H peak	30 mW

rms could be maintained during runs lasting 10 h.

Studies of Stark-assisted one-photon transitions indicate that the stray electric fields are not uniform in amplitude within the interaction volume. Because of this complicating factor, it was felt that the most reliable way to measure and correct for the effects of these small fields was through direct observation of the Stark shifts caused in one of the EFS resonances. For sufficiently small values of the stray field, the Stark shifts of all the $n=10$ Rydberg states are proportional to the mean-square stray electric field, with proportionality coefficients which may be calculated reliably. That is, the energies can be written as

$$\begin{aligned} E_M(E^2)&=E_M^0+b_M E^2 ,\\ E_L(E^2)&=E_L^0+b_L E^2 ,\\ E_K(E^2)&=E_K^0+b_K E^2 ,\\ E_I(E^2)&=E_I^0+b_I E^2 ,\\ E_H(E^2)&=E_H^0+b_H E^2 . \end{aligned} \tag{5}$$

The average Stark shift rate, assuming statistical population of all the $|m_J|\leq 5$ levels, are [in units of MHz/(V/cm)^2] $b_M=+112$, $b_L=-10$, $b_K=-42$, $b_I=-34$, and $b_H=-19$. Since the $10M$ state is by far the most sensitive to Stark shifts, we abandoned hope of measuring its position and used it instead as a measure of the stray electric fields. We measured experimentally the four intervals H-I, I-K, K-L, and K-M. The last interval, observed by two-photon spectroscopy, was designed to monitor the stray electric field. By *assuming* a value for the zero-field $10K$-$10M$ interval

$$\nu_{KM}^0=E_M^0-E_K^0 , \tag{6}$$

the average value of the stray electric field could be inferred from the measured value of the K-M interval $\nu_{KM}^{\rm OBS}$, that is,

$$E^2=(\nu_{\rm KM}^{\rm OBS}-\nu_{KM}^0)/(b_M-b_K) . \tag{7}$$

Then the field-free values of the other intervals could be inferred from the observed intervals and the calculated relative Stark shift rates,

$$\begin{aligned} \nu_{KL}^0&=\nu_{KL}^{\rm OBS}-\left[\frac{b_L-b_K}{b_M-b_K}\right](\nu_{KM}^{\rm OBS}-\nu_{KM}^0) ,\\ \nu_{IK}^0&=\nu_{IK}^{\rm OBS}-\left[\frac{b_K-b_I}{b_M-b_K}\right](\nu_{KM}^{\rm OBS}-\nu_{KM}^0) ,\\ \nu_{HI}^0&=\nu_{HI}^{\rm OBS}-\left[\frac{b_I-b_H}{b_M-b_K}\right](\nu_{KM}^{\rm OBS}-\nu_{KM}^0) . \end{aligned} \tag{8}$$

Although this procedure does require the assumption of a value for ν_{KM}^0, an interval which has never been measured, the fact that the factors in brackets in the preceding equations are much less than one makes the eventual results rather insensitive to the assumed value. The bracketed factors are themselves slightly uncertain (by approximately 20%) due to their dependence on the distribution of m_J states which contribute to each resonance.

In order to allow for the possibility that the stray electric field varies with time, measurements of the K-M resonance were interspersed periodically among the measurements of the other resonances. The centers of the K-M resonance were observed to change very little over a 10-h time scale.

The second major systematic effect in these measurements is due to imperfect impedance matching at the exit port of the TEM rf transmission line, which forms the spectroscopy region. As a result of this mismatch, while the rf traveling wave is nominally propagating parallel to the atomic beam, there is a weaker reflected wave propagating antiparallel to the beam, and vice versa. In the rest frame of the moving atoms, these two traveling waves have different frequencies, resulting in a distortion of the resonance line shape.

The effect of the weak counter-propagating wave on the resonance line shape for a two-level transition resonance may be calculated in various approximation schemes. The simplest approach is appropriate when both traveling waves are weak enough to be treated by perturbation theory. Under these circumstances, the resonance line shape is predicted to be

$$S_{\pm}(\nu)=\left|\frac{\sin[\nu^0-\nu(1\mp\beta)]\pi T}{[\nu^0-\nu(1\mp\beta)]\pi T}+|\Gamma|e^{i\theta}\frac{\sin[\nu^0-\nu(1\pm\beta)]\pi T}{[\nu^0-\nu(1\pm\beta)]\pi T}\right|^2 , \tag{9}$$

where the reflection coefficient, measured at the center of the transmission line, has magnitude $|\Gamma|$ and phase θ, and $S_{\pm}(\nu)$ is the predicted line shape for the case when the primary propagation direction of the microwaves is parallel $(+)$ or antiparallel $(-)$ to the atomic beam velocity. Figure 7 shows resonance line shapes calculated from this formula for the two cases, assuming that they are characterized by equal reflection coefficients. If resonance lines of this form are fit to a simple symmetric function, the apparent center of the dominant feature will be shifted upwards in one case and downwards by an equal amount in the other. The average of the two fitted centers is unchanged from the result that would be found from similar profiles with $|\Gamma|=0$.

This feature of the line-shape distortions due to the weak reflected wave is the basis of the procedure which has been used to eliminate their effects on the precision measurements of the EFS intervals. Two resonances, resembling the simulations of Fig. 7, may be obtained by simply reversing the direction of propagation of the primary rf traveling wave in the spectroscopy region. However, in this case, the reflections of concern are being produced by opposite ends of the transmission line, and may therefore be slightly different in magnitude or phase due to physical differences in the nominally identical ends of the transmission line. Any such difference, however, can itself be reversed in sign by physically rotating the transmission line so that its two ends are encountered in reverse order by the atomic beam. This leads naturally to

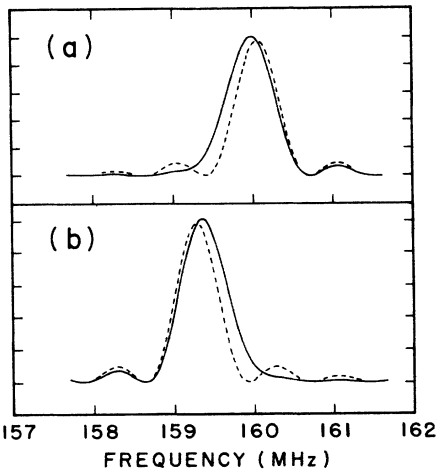

FIG. 7. Simulations of reflected wave effects. The dashed curves are the line shape in the absence of a reflected wave. The solid curves include reflected wave effects for rf propagation in the same direction (a) and in the opposite direction (b) as the beam. The curves shown are for large reflection coefficients ($\Gamma=-0.3$) in order to emphasize the line-shape distortion. Note that the distortion in (a) causes an apparent shift which is of the same amplitude, but of the opposite direction as the shift due to the distortion in (b).

the consideration of the four "configurations" of the resonance apparatus specified in Table II. The final column of Table II indicates the apparent center of a single component resonance obtained in each configuration. The quantity ϵ_1 (ϵ_2) is the line center shift due to the weak wave reflected from end 1 (end 2) of the transmission line. Within this model, two linear combinations of the results in the four configurations will give the correct, unshifted line center

$$\nu^0=(\nu_A+\nu_D)/2=(\nu_C+\nu_D)/2\ . \tag{10}$$

Differences between the results in the various configurations were used to determine the size of the shift due to the reflected wave and to check for differences between the two ends of the transmission line. (No significant difference was found.)

This general approach was used throughout the experiment to monitor and eliminate the effects of these weak reflected waves on the measurements. Data for all the resonances were taken in all four configurations of Table II. In addition, a more detailed theoretical study, incorporating both the complications due to the presence of more than one resonance component in the spectrum and a more complete calculation of the lineshape distortion including the effects of saturation of the transitions, has been carried out, with the result that corrections to this simple procedure are very small.

III. MEASUREMENTS

The electric-fine-structure-interval measurements reported here are based on data accumulated during six independent "runs," during each of which all three transitions $10H$-$10I$, $10I$-$10K$, and $10K$-$10L$ were measured at least three times in each of the four configurations of Table II, with measurements of the $10K$-$10M$ interval repeated throughout the run as a check on stray electric fields. In all, these data represent more than 1000 h of data collection. The measurements of each resonance were taken under computer control, with an Apple IIe microcomputer setting the microwave frequency (generated by a Hewlett-Packard 8670C Microwave Synthesizer) to a predetermined sequence of measurement frequencies across the resonance and recording, at each frequency, the average signal over a 30-sec measurement period. The data plotted in Fig. 6(b) and 6(c), for instance, represents the average of 12 such resonance scans, so that each plotted point represents 6 min of integration time.

The six "runs" differed in several ways, as a partial check against unanticipated systematic errors, as listed in Table III. Most of the runs were taken with an atomic beam energy of 11.20(2) keV, but two were taken with altered beam energy. For two of the runs, the frequencies chosen for the pre-pump and post-pump regions were altered, which in turn altered the relative intensities of the four MFS components in the I-K and K-L transitions. For the last run, the rf interaction region was completely disassembled and reassembled in such a way that its impedance was substantially altered as a check on the treatment of reflection effects. Finally, most of the runs studied only one component of the $10H$-$10I$ transition, the well-resolved $10^-H_5-10^-I_6$ transition. The last run, however, included all four components, as illustrated in Fig. 6(a).

For each run, the measured resonance curves were fit to a function of the form given in Eq. (4), with the positions of the four resonance components relative to the "pure" EFS interval fixed from the MFS theory, as given in Fig. 1.[1] Allowed to vary in the fit were the amplitudes of the four components and the (Doppler shifted) EFS interval. With the standard-deviation measurement errors of the measured signal estimated from the scatter of re-

TABLE II. The four geometries in which the line centers were measured. The corrections to the line centers are due to the Doppler shift and the reflected wave. β is the beam speed and ϵ_1 and ϵ_2 are the reflected wave shifts due to the two ends of the rf interaction region.

Configuration	rf propagation	rf region	Line center
A	copropagating	normal	$\nu_0(1+\beta+\epsilon_1)$
B	counterpropagating	normal	$\nu_0(1-\beta-\epsilon_2)$
C	copropagating	reversed	$\nu_0(1+\beta+\epsilon_2)$
D	counterpropagating	reversed	$\nu_0(1-\beta-\epsilon_1)$

TABLE III. Experimental conditions for the six runs of the experiment. Errors are given in parentheses.

Run	Accelerating voltage	*HI* scans	*H-I* pump frequency	*H-K* pump frequency	Γ
1	11.18(1) kV	1 peak	157.0 MHz	112.0 MHz	Γ_1
2	11.18(1) kV	1 peak	157.0 MHz	112.0 MHz	Γ_1
3	10.13(1) kV	1 peak	157.0 MHz	112.0 MHz	Γ_1
4	12.16(1) kV	1 peak	157.0 MHz	112.0 MHz	Γ_1
5	11.22(1) kV	1 peak	159.5 MHz	110.0 MHz	Γ_1
6	11.22(1) kV	4 peaks	159.5 MHz	110.0 MHz	Γ_6

peated measurements at the same frequency, the signals were found to be fit satisfactorily by Eq. (4). The uncertainty in the fitted EFS interval was therefore estimated by propagation of the signal-measurement errors.

Table IV shows the average fitted EFS interval for each of the six experimental runs of Table II, together with the estimated statistical error. Also shown in each case is the average correction to be applied as a result of Stark shifts due to stray fields, as inferred from measurements of the K-M interval throughout the run. The errors shown for these corrections are purely statistical, derived from the measurement errors in the K-M interval. Additional systematic errors associated with this procedure will be treated later. Corrected for Stark shifts, the six runs give six independent measurements of each of the three intervals. The scatter of these independent measurements is slightly greater than would be expected on the basis of the errors derived from the fits. We therefore expand the statistical error in the mean result to reflect the actual scatter in the independent measurements.

Table V summarizes the systematic corrections and uncertainties associated with the determination of the three EFS intervals. The first row gives the mean results from Table IV. The largest systematic uncertainties come from the dc Stark shift correction, and are of three types. First, there is the error associated with the uncertainty in the assumed value of $\nu^0_{KM}+\Delta_{\rm MFS}$ for a particular interval (the $10^-K_7-10^-M_9$) which was used to monitor the stray field. The calculation of Drachman[2] predicts $\nu^0_{KM}=40.7957(2)$ MHz. To be on the conservative side, we will assume here that $\nu^0_{KM}=40.7957(6)$ MHz. Reference 1 gives $\Delta_{\rm MFS}=1.8227$ MHz with the largest uncertainty being due to an unresolved discrepancy of order m_e/M_α. We take 0.8 kHz as a conservative estimate of the error on $\Delta_{\rm MFS}$. Propagating these errors through Eq. (8) leads to the uncertainties shown in Table V. An additional source of uncertainty in this correction comes from the fact that the measured position of the K-M resonance is affected by ac Stark shifts. Given the strength of the rf

TABLE IV. Average fitted EFS intervals for each of the six runs. The values in the third column represent the average of the centers of twelve scans (three in each of the experimental geometries of Table II). The dc shifts are given in the fourth column along with their statistical errors. The corrected values are given in the final column. All values are in MHz. Errors are given in parentheses.

EFS interval	Run number	Average of A, B, C, and D	dc shift	Corrected interval
H-I	1	157.0495(25)	+0.0065(6)	157.0560(26)
H-I	2	157.0483(25)	+0.0027(6)	157.0510(26)
H-I	3	157.0499(25)	+0.0001(6)	157.0500(26)
H-I	4	157.0514(26)	+0.0004(6)	157.0518(24)
H-I	5	157.0531(23)	+0.0029(6)	157.0560(26)
H-I	6	157.0528(22)	+0.0050(6)	157.0578(23)
I-K	1	60.8180(18)	+0.0025(3)	60.8205(18)
I-K	2	60.8138(18)	+0.0008(3)	60.8146(18)
I-K	3	60.8183(22)	+0.0001(3)	60.8184(22)
I-K	4	60.8195(17)	+0.0003(3)	60.8198(17)
I-K	5	60.8192(19)	+0.0014(3)	60.8206(19)
I-K	6	60.8200(19)	+0.0025(3)	60.8225(19)
K-L	1	27.1780(33)	−0.0110(10)	27.1670(34)
K-L	2	27.1771(33)	−0.0039(10)	27.1732(34)
K-L	3	27.1772(33)	−0.0002(10)	27.1770(35)
K-L	4	27.1796(34)	−0.0010(10)	27.1786(36)
K-L	5	27.2024(48)	−0.0053(10)	27.1971(49)
K-L	6	27.1956(34)	−0.0090(10)	27.1866(36)

TABLE V. The systematic errors and corrections to the EFS intervals. All values are in MHz. Errors are given in parentheses.

	H-I	*I-K*	*K-L*
Average of Table VI	157.0538(13)	60.8194(11)	27.1799(43)
dc shift systematic errors			
K-M interval uncertainty	0.0000(1)	0.0000(1)	0.0000(2)
ac shift uncertainty	0.0000(18)	0.0000(9)	0.0000(37)
Shift rate uncertainty	0.0000(6)	0.0000(3)	0.0000(10)
Line-shape uncertainty	−0.0012(12)	−0.0041(10)	+0.0029(25)
Residual reflection effects	−0.0007(3)	+0.0001(0)	+0.0007(3)
Effect due to fitting $m=3$ only	−0.0004(4)	+0.0004(4)	+0.0004(4)
Time dilation	−0.0005(0)	−0.0002(0)	−0.0001(0)
ac Stark shifts	−0.0002(1)	−0.0004(1)	−0.0003(1)
Linear power variation	0.0000(0)	0.0000(0)	0.0000(0)
Corrected EFS intervals	157.0508(26)	60.8152(18)	27.1835(63)

electric fields inside the interaction region, these can be calculated.[16] Alternatively, they can be inferred experimentally by extrapolating the measured *K-M* resonance to zero rf power. The two approaches give consistent results and indicate that the measured *K-M* interval should be corrected downward by

$$\Delta_{KM} = -0.074(18)\ \text{MHz} . \tag{11}$$

The rf electric field inside of the meter-long interaction region is expected to vary from run to run due to slight changes in alignment. Thus the ac shift would also be expected to vary. We made measurements of the ac shift on three separate days and found no evidence for this variation. Nevertheless, we expanded the estimated error on the ac shift to allow for the possibility of this variation. A varying ac shift could explain why the scatter of Table IV is somewhat larger than the statistical errors. The error in this ac shift correction in ν_{KM}^{OBS} translated into the uncertainty in the average Stark shift correction is shown in Table V. Finally, the uncertainties in the coefficients "*b*," due to lack of knowledge of the distribution of m_J states which make up the signal, is estimated to be ±20%, leading to the uncertainties shown.

A second important systematic effect is related to uncertainty in the detailed shape of the measured resonance line shape. In writing Eq. (3), we assumed that the rf electric field has a uniform amplitude and a duration T. From the field geometry and known beam speed the experimentally appropriate value of T (1.34 μsec) is known to within 1%. While the individual resonance scans are satisfactorily fit by a line shape of the form of Eq. (3) with $T=1.34$ μsec, consideration of several such scans clearly shows that the observed lines are broader (by about 7%) than Eq. (3) predicts. This discrepancy cannot be accounted for by the simplifying assumptions used in arriving at Eq. (3), nor can it be attributed to inaccuracy in the measurement of the beam velocity or field length. One plausible explanation for the broadening is the nonuniformity of the rf field amplitude within the interaction region due to bowing of the center conductor or misalignment of the beam.

It would be a simple matter to artificially decrease the parameter T in Eq. (3) in order to obtain a better fit of the experimental line shapes. However, this process would also change the line shape in the far wings where the data is not conclusive about the correct shape. Because of the overlap of the several resonance components, an error in the off-resonance line shape could shift the apparent centers of the resonances. Without a firm understanding of the physical mechanism responsible for the additional broadening, there is no unique way to modify the line shape. On the other hand, to fit the data using Eq. (3) and $T=1.34$ μsec is to use a line-shape function which is clearly inconsistent with the measured line shapes. We chose to handle this problem by fitting the data to a variety of functional forms which allow for slight broadening of the line shape while affecting the off-resonance line shape in different ways. We found that the broader lines gave slightly different results for the EFS intervals than were found using Eq. (3) and $T=1.34$ μsec. There was, however, relatively little sensitivity to the method of broadening. In order to emphasize the dependence of the results on this rather *ad hoc* procedure, we treat the alteration of the fitted centers caused by fitting them with the broadened lines as a *correction* and enter it in the fifth row of Table V. The uncertainties in these corrections are derived from the sensitivity of the results to the precise form of broadening used. That is, they represent uncertainties due to ignorance of the exact line shape.

There are several other small systematic corrections which have been calculated. First, there is a residual error due to the reflected wave in the rf interaction region, which remains after averaging over the four configurations of Table II. This has been estimated by fitting simulated line shapes which incorporate reflection effects at the level which accounts correctly for the observed differences between the results in the several configurations. Secondly, there is a small correction due to the fact that the fitting function includes only $m_J=3$ line-shape functions, and therefore does not correctly compensate for the partially overlapping resonances. This correction was calculated by fitting simulated reso-

TABLE VI. Comparison of present measurement to previous measurements and to theory. The first two rows show the previous and present experimental measurements. The theory of Drachman (Ref. 2) excluding retardation effects is given in the third row. The fourth row is the difference between experiment and the third row and is thus an estimate of the retardation effects. The calculated retardation effects of Au, Feinberg, and Sucher (Ref. 8) are given in the fifth row. All values are in MHz. Errors are given in parentheses.

	G-H	*H-I*	*I-K*	*K-L*
Previous measurement[a]	490.990(10)	157.068(13)	60.818(10)	
Present measurement		157.0508(26)	60.8152(18)	27.1835(63)
Theory excluding retardation[b]	491.01(52)	157.057(10)	60.8183(4)	27.1759(2)
E-T (estimate of retardation effects)	−0.02(52)	−0.006(10)	−0.0031(18)	+0.0076(63)
Calculated retardation effects	−0.04	−0.012	−0.0045	−0.0018

[a]Reference 6.
[b]Reference 2.

nances, assuming a statistical distribution of $|m_J| \leq 5$ states.

Additional small corrections, shown in Table V, are due to (a) time dilation, (b) ac Stark (and Bloch-Siegert) shifts,[16] and (c) possible linear variation of the microwave power with frequency of $0\pm0.05\%$ per MHz. The final corrected values of each of the EFS intervals are shown in the final row of Table V.

IV. DISCUSSION OF RESULTS

Table VI summarizes the measurements reported here, and compares them to the results of earlier measurements. Satisfactory agreement is found with the results of Palfrey,[6] which are about an order of magnitude less precise than the present measurements. The theoretical predictions of Drachman[2] (excluding any retardation effects) and their estimated uncertainties obtained by considering the convergence of the polarization potential series are shown in the third row. Subtracting these predictions from our experimental results gives an estimate for the retardation effects. These estimates are shown in the fourth row and can be compared directly to the theoretical predictions of Au, Feinberg, and Sucher for the retardation effects[8] which are given in the fifth row. Comparison of these two rows show that our measurements are completely consistent with theoretical predictions. The most significant result comes from the 10*I*-10*K* interval for which the retardation effects are estimated to be -3.1 ± 1.8 kHz. This result is in good agreement with theory, and, while it is not very conclusive evidence for the presence of retardation effects, it appears to be the best evidence available to date. It can be seen from Table VI that for both the *G-H* and *H-I* intervals the experimental precision is already considerably smaller than the predicted retardation effects, but the uncertainty in the theoretical calculations of the intervals prevents a meaningful test of the predictions.

The precision of the present measurements is limited approximately equally by statistical and systematic errors, with the primary systematic errors being associated with (a) the procedure for correcting for dc shifts and (b) the influence of line-shape uncertainties in fitting compound resonances. In future measurements, it should be possible to reduce the uncertainties due to these systematic effects, and work is now under way to improve the experimental apparatus with this aim. If comparable improvements in statistical errors can also be achieved, it should be possible to attain measurement precision approaching 0.1 kHz in future measurements of these intervals.

On the theoretical side, there are still a number of open questions for which additional calculations could be helpful in clarifying the physics of the high-L states. One weakness of existing calculations of these states is that the magnetic fine structure, including both spin and exchange effects, is not included in the most precise calculations.[2] The separate treatment of magnetic fine structure given in Ref. 1 is adequate for the present measurement, but it is unreliable at the level which will be required by improved measurements. Contributions to the MFS of relative order m_e/M_α are uncertain due to an unresolved discrepancy between different calculations, and terms of relative order α^2 are uncertain due to uncalculated relativistic corrections. Some progress on the relativistic treatment of the MFS has been made recently by Idrees.[17] The exchange energies for the high-L states are ignored in the treatments of Refs. 18 and 2 and are treated as a parameter in Ref. 1. In fact, the exchange energies for $L > 4$ states have never been reliably calculated. They are expected to be very small, and have been taken to be exactly zero for the analysis of this experiment. It would be preferable to have theoretical values as has been achieved for the lower-L states.[19,20] In general, the theoretical understanding of the high-L helium Rydberg states, while apparently adequate to account for existing measurements, consists of a collection of partial calculations with various starting points. If possible, it would be desirable to achieve a more complete calculation based consistently on first principles.

ACKNOWLEDGMENTS

We would like to acknowledge the work of David Van Baak, Francis Deck, and Jim Hammons in the earlier stages of this experiment. This work has been supported by the National Science Foundation under Grant No. PHY87-09707.

[1]E. A. Hessels, W. G. Sturrus, S. R. Lundeen, and David R. Cok, Phys. Rev. A **35**, 4489 (1987).
[2]Richard J. Drachman, Phys. Rev. A **31**, 1253 (1985).
[3]J. W. Farley, K. B. MacAdam, and W. H. Wing, Phys. Rev. A **20**, 1754 (1979); J. W. Farley *et al., ibid.* **25**, 1559 (1982); H. Wing and K. B. MacAdam, in *Progress in Atomic Spectroscopy,* edited by W. Hanle and H. Kleinpoppen (Plenum, New York, 1978), p. 491.
[4]H. J. Beyer and K. J. Kollath, J. Phys. B **11**, 979 (1978).
[5]David R. Cok and S. R. Lundeen, Phys. Rev. A **23**, 2488 (1981).
[6]S. L. Palfrey and S. R. Lundeen, Phys. Rev. Lett. **53**, 1141 (1984).
[7]Edward J. Kelsey and Larry Spruch, Phys. Rev. A **18**, 15 (1978).
[8]C. K. Au, G. Feinberg, and J. Sucher, Phys. Rev. Lett. **53**, 1145 (1984).
[9]H. B. G. Casimir and D. Polder, Phys. Rev. **73**, 360 (1948).
[10]H. B. G. Casimir, Proc. Ned. Akad. Wet. **51**, 793 (1948).
[11]Larry Spruch and Edward J. Kelsey, Phys. Rev. A **18**, 845 (1978); Larry Spruch, Phys. Today **39**(11), 37 (1986).
[12]T. N. Chang and R. T. Poe, Phys. Rev. A **14**, 11 (1976).
[13]James F. Babb and Larry Spruch, Phys. Rev. A **36**, 456 (1987).
[14]C. W. Fabjan and F. M. Pipkin, Phys. Rev. A **6**, 556 (1972).
[15]S. L. Palfrey, Ph.D. thesis, Harvard University, 1983.
[16]J. R. Brandenberger, S. R. Lunden, and F. M. Pipkin, Phys. Rev. A **14**, 341 (1976).
[17]M. Idrees, Bull. APS, **33**, 1040 (1988).
[18]G. Feinberg, J. Sucher, and C. K. Au, Ann. Phys. (N.Y.) **173**, 355 (1987).
[19]James Sims and W. C. Martin, Phys. Rev. A **37**, 2259 (1988).
[20]G. W. F. Drake, Phys. Rev. Lett. **59**, 1549 (1987).